An *in vitro* model for early anteroposterior organisation during human development

Naomi Moris[1,*] †, Kerim Anlas[1,2]†, Susanne C. van den Brink[3]†, Anna Alemany[3]†, Julia Shroeder[1,4], Sabitri Ghimire[1], Tina Balayo[1,5], Alexander van Oudenaarden[3,#] & Alfonso Martinez Arias[1,*,#]

1. Department of Genetics, University of Cambridge, Cambridge, UK, CB2 3EH
2. Present address: EMBL, 08003 Barcelona, Spain
3. Oncode Institute, Hubrecht Institute-KNAW (Royal Netherlands Academy of Arts and Sciences) and University Medical Center Utrecht, 3584 CT, Utrecht, The Netherlands
4. Present address: Heidelberg University, Grabengasse 1, 69117 Heidelberg, Germany
5. Present address: Universidad de las Palmas de Gran Canaria (ULPGC), 35016 Las Palmas de Gran Canaria, Las Palmas, Spain

†. These authors contributed equally

** Authors for correspondence: nem33@cam.ac.uk , ama11@hermes.cam.ac.uk and a.vanoudenaarden@hubrecht.eu*

[#] *These authors jointly supervised this work*

The body plan of the mammalian embryo is shaped through the process of gastrulation, an early developmental event that transforms an isotropic group of cells into an ensemble of tissues ordered with reference to three orthogonal axes[1]. While model organisms have provided much insight into this process, we know very little about gastrulation in humans due to the difficulty of obtaining embryos at such early stages of development, as well as to the ethical and technical restrictions that limit the feasibility of observing gastrulation *ex vivo*[2]. Here we show that human embryonic stem cells can be used to generate gastruloids: three dimensional multicellular aggregates that differentiate to derivatives of the three germ layers organised spatiotemporally, without additional extra-embryonic tissues. Human gastruloids undergo elongation along an anteroposterior axis and, using spatial transcriptomics, we show that they exhibit patterned gene expression. This includes a somitogenesis signature that suggests that 72 hour human gastruloids exhibit features of Carnegie Stage 9 embryos[3]. Our study represents a new, experimentally tractable model system to reveal and probe human-specific regulatory processes occurring during axial organisation in early development.

The body plan of mammalian embryos emerges through interactions of sequential cell fate decisions and morphogenetic events, which have hitherto been difficult to observe in humans. Human Embryonic Stem Cells (hESCs)[4] have opened up opportunities for studying early fate decisions, and have hinted at the existence of regulatory mechanisms specific to humans[5,6]. But, in contrast to the embryo, where proportionate populations interact with one another to generate tissues and organs, differentiation in adherent culture is heterogeneous and favours a limited number of cell types[7]. Seeding hESCs on micropatterned surfaces yields coordinated patterns of gene expression, but without the axial organization characteristic of embryos[8]. However, when mouse ESCs are aggregated in suspension under defined conditions, they generate 'gastruloids': a three-dimensional, *in vitro* model of mammalian development, which exhibits an embryo-like spatiotemporal organization of gene expression[9,10]. We hypothesised that similar human gastruloids could be derived from hESCs.

Generation of human gastruloids

When hESCs in 2D culture were treated with Chiron, a Wnt agonist, for one day before seeding defined numbers in low-adherence plates in the presence of Chiron, they formed compact, spherical aggregates within a few hours (Fig. 1a, Extended Data Fig. 1a-c). These aggregates progressively broke symmetry and formed elongated structures, with maximal elongation at 72-96h (Fig. 1a-d). On average, ~66% of aggregates from each experiment displayed an elongated morphology at 72h. Although some of the structures remained

elongated until 96h, the majority tended to curl or retract after 72h (Fig. 1e and Extended Data Fig. 1d; see Methods for details of classification). Different cell lines required different concentrations of Chiron stimulation (Extended Data Fig. 1e).

Before aggregation, pre-treated hESCs were found to express pluripotency markers but with increased expression of mesendodermal marker genes including BRA, MIXL1, EOMES (Extended Data Fig. 2a; Supplementary Table 1) and membrane localised CDH2 (N-Cadherin) (Extended Data Fig. 2b-d). These results suggest that following Chiron pre-treatment, hESCs become partially primed towards a primitive streak-like state, in agreement with observations that Wnt signalling induces mesodermal differentiation of hESCs[7,11].

Axial organisation of gene expression

Polarised expression of BRA protein was detectable as early as 24h (Extended Data Fig. 3a) overlapping a SOX2 expressing domain which, by 96h, had resolved into distinct BRA+ and SOX2+ expressing regions (Fig. 1g). All cells exhibited CDH2 expression with higher levels in the posterior BRA+ and SOX2+ domain (Fig. 1g; Extended Data Fig. 3b). A group of GATA6 expressing cells were localized at one end, opposite to cells expressing CDX2 (Fig. 1g) and this pattern was refined as the aggregates underwent elongation (Extended Data Fig. 3c-f; see Methods for details of classification). The polarisation of GATA6 was confirmed using live-imaging of a S4-GATA6 reporter line[12] and occurred as early as 24h (Supplementary Video 1 and Extended Data Fig. 3g). The CDX2 expressing region also contained BRA expressing cells (Fig. 1g), suggesting a correspondence to posterior embryonic identity, since co-expression of these genes is restricted to the tailbud of mammalian embryos.

To ascertain whether human gastruloids were capable of generating derivatives of the three germ layers, we made use of a reporter line (RUES2-GLR[13]) to identify progenitors for the mesoderm (BRA), endoderm (SOX17) and neuroectoderm (SOX2) (Fig. 2a). Time lapse video of RUES2-GLR during aggregation (Supplementary Video 2) and elongation (Supplementary Video 3) allowed us to follow the process of symmetry-breaking and segregation of germ layer progenitors. Initially, all cells express SOX2 (Fig. 2b) before individual SOX17+ cells emerge throughout the aggregate and SOX2 expression becomes confined to one end of the aggregates (Fig. 2c). Between 24-48h, BRA expression, initially low and ubiquitous, increases and becomes localised to the SOX2 expressing region of the aggregate. By 72h, aggregates expressed BRA at the distal end, with neighbouring SOX17 and SOX2 expressing domains (Fig. 2d). The profiles of these fluorescent reporter genes were comparable among individual gastruloids when aligned along their AP axis (Fig. 2e).

The Chiron pre-treatment was absolutely necessary for elongation and patterned gene expression (Fig. 1d and Extended Data Fig. 1a-b). However, in our experiments, Wnt3a pre-treatment was unable to substitute for Chiron, as evidenced by a lack of elongation and absence of BRA expression (Extended Data Fig. 4a), suggesting differential effects between Chiron and Wnt3a in hESCs[14]. We also found that BMP4, which is used to trigger patterned gene expression in micropatterns[8], was unable to substitute for Chiron and led to small, spherical aggregates with no discernible patterning (Extended Data Fig. 4b). These observations highlight differences in the cellular response to signals, perhaps associated with the dimensionality of the system. They also suggest that the formation of human gastruloids is highly dependent on the signalling exposure of the initial cell population.

To investigate further the dependence of human gastruloid formation on signalling, we applied small molecule inhibitors of BMP, Wnt and Nodal signalling during pre-treatment. When RUES2-GLR cells were exposed to routine levels of Chiron in the presence of BMP (LDN193189) or Wnt (XAV-939) inhibition, hESCs were not able to form patterned aggregates or to elongate (Extended Data Fig. 4c). Likewise, inhibition of Nodal signalling (SB431542; "SB43") led to ovoid aggregates that co-express both SOX2 and BRA (Extended Data Fig. 4d), though increasing the concentration of Chiron during aggregation elevated BRA expression and led to robust elongations, with co-expression of BRA and SOX2 at the posterior pole (Extended Data Fig. 4d). These results suggest that a balance between the levels of Nodal and Wnt/ß-catenin signalling plays a role in establishing fate decisions and promoting elongation in human gastruloids.

Having observed this signal-dependence during human gastruloid formation, we examined the effect of sustained gastruloid culture with Retinoic Acid (RA), known to disrupt axial patterning and cause congenital malformations[15]. RA treated gastruloids were typically rounded and exhibited high SOX2 expression, with a strong reduction in BRA expression, although they had separate domains of CDX2 and GATA6 (Extended Data Fig. 4e-f). This suggests that certain elements of axial patterning and organisation, particularly elongation, were adversely affected by RA application in the human gastruloids.

These results support the notion that the signalling environment, before and during gastruloid development, is a critical factor in establishing both the morphology and patterning of human gastruloids.

A transcriptional body plan in human gastruloids

To explore the transcriptional complexity of human gastruloids, we applied tomo-sequencing (tomo-seq)[16] to 72h Chiron pre-treated RUES2-GLR gastruloids (Methods). Two replicates were embedded and sectioned along their AP axis, before RNA-seq processing each of the sections (Fig. 3a-b and Extended Data Fig. 5a; Methods).

We found 1,023 genes that were reproducible between the two replicates (Methods), organised into 22 main classes of expression patterns with representatives of all three germ layers (Fig. 3c-e and Extended Data Fig. 5b-c, Supplementary Data 1-2). Most notably, six clusters, localised to the posterior-most region of the gastruloid (Clusters 0-5), contained genes whose homologues are localized in the tailbud of mouse embryos, including BRA, CDX2, and CYP26A1. At the opposing end, we observed 9 clusters (Clusters 6-14), containing genes associated with cardiac and anterior endoderm development in the mouse embryo, including KDR, MEIS1/2, PBX1, TWIST1, ISL1, IRX1/2/3 and PRDM1 (Supplementary Data 3; Fig. 3c, d). Cluster 21 was strongly enriched for genes involved in somitogenesis and the Notch signalling pathway.

We did not find evidence for the expression of genes associated with the development of anterior neural structures (Extended Data Fig. 6a) but observed expression of many paralogues from the 4 HOX clusters (Extended Data Fig. 6b). In mouse embryos, *Hox* genes are known to be sequentially expressed along the anteroposterior axis. In human gastruloids, HOX genes exhibit variable expression domains along the length of the gastruloid AP axis, but display a somewhat broader domain of paralogues 1-5, and more posterior-biased distribution of groups 6-8. Paralogues 9-13 were variably or lowly/not expressed (Fig. 3f and Extended Data Fig. 6b). Some posterior genes also exhibited expression in the anterior part of the gastruloid (e.g. HOXA9-10 and HOXC9-10; Fig. 3f). Currently, in the absence of an embryonic reference it is not possible to discern whether this localization reflects an early phase in the regulation of HOX gene expression, a species difference or a feature of this model system.

These global patterns of gene expression raised the question of whether this organization reflects elements of a body plan, the blueprint for the organism. This possibility is supported by the organization of a posterior domain of gene expression in the human gastruloids (Fig. 4a-b), where we observed a node-like transcriptional domain (Fig. 4c-d, Extended Data Fig. 6c)[17]. At the anterior end, we observed the polarisation of genes associated with cardiac mesoderm development (Fig. 4e-f)[18,19].

148

Signalling and Pattern Organisation

150 One of the mechanisms by which gastruloids might establish or maintain patterning along their AP axis includes the organization of signalling components along their length. Assessing this
152 in the tomo-seq data, we observed a number of Wnt ligands preferentially expressed at the posterior-end (WNT5A, WNT3A, WNT5B, LEF1 and WNT3) and some BMP ligands anteriorly
154 (BMP2, BMP4 and BMP5; Extended Data Fig. 6d). Using a BMP/SMAD1 reporter line[20], we observed increased nuclear SMAD1-RFP at the anterior end (Extended Data Fig. 6e-f).
156 Anterior BMP signalling localisation is consistent with its function in cardiac development of the mammalian embryo. At the posterior end we observed expression of WNT3a and LEF1,
158 indicating Wnt signalling within the posterior region (Extended Data Fig. 6g-h). Additionally, we observed a peak of Nodal signalling components and targets, including NODAL, LEFTY1/2
160 and CER1, within the posterior region of human gastruloids (Extended Data Fig. 6i). This is consistent with a known role of Wnt and Nodal signalling in the mammalian tailbud, and
162 together suggests that human gastruloids might utilise signalling gradients along their AP axis to establish patterning.

164

In mouse embryos, Nodal signalling plays an early role in establishing different fates along the
166 AP axis, before becoming localized to the posterior pole and the node[21,22]. Having observed that suppression of Nodal signalling during pre-treatment could still lead to robust elongation
168 of human gastruloids (Extended Data Fig. 7a-b and Extended Data Fig. 4d), we wanted to examine the organization of gene expression in these gastruloids closely. Gastruloids pre-
170 treated with Chiron and SB43 displayed a larger, well-defined SOX2 domain at their posterior end, diffuse expression of BRA that approximated an anteroposterior gradient, and an
172 absence of detectable SOX17 expression (Extended Data Fig. 7b-d; Supplementary Table 2). Comparative analysis between 120h Chiron and SB43 pre-treated gastruloids and those
174 without Nodal-signalling inhibition (Extended Data Fig. 7d-g and Extended Data Fig. 8a-c, Supplementary Data 4-5 and Methods) showed that although 301 genes were reproducibly
176 localised in both conditions, SB43 treatment led to the acquisition of 944 genes with novel spatial localisation, and the loss of reproducible localisation of 509 genes (Extended Data Fig.
178 7e; Supplementary Data 5). Additionally, 564 genes (33%) were differentially expressed between the two treatments (Extended Data Fig. 7f and Supplementary Data 6). One cluster
180 of genes lost on SB43 pre-treatment (Cluster 4; Extended Data Fig. 7g) included genes known to be involved in Nodal signalling and many associated with the node in mammalian embryos
182 (Supplementary Data 5), consistent with a loss of Nodal activity. We also noticed a decrease in expression of genes associated with definitive endoderm (SHH, LHX1, CER1, FOXA3,
184 SORCS2, FOXA2) consistent with a role of Nodal in the specification of this germ layer in

mouse embryos[21], and a loss of genes associated with cardiac development (TBX5, GATA6, LBX1, NKX2.5) likely to be a consequence of the loss of induction from the endoderm[23] (Extended Data Fig. 8d, e and Supplementary Data 7).

Together, these observations indicate that the spatial organization of signalling molecules, and their activity in human gastruloids, mirror those of mammalian embryos.

Comparative spatial transcriptomics

The high degree of organization in gene expression that we observed in human gastruloids prompted us to explore the correspondence of these patterns with other developmental models. To do this, we focused on mouse gastruloids as an equivalent model system[9,10]. The comparison of tomo-seq datasets showed a high degree of conservation in axial patterning (Fig. 4g and Supplementary Data 8). In particular we observed a conserved pattern of mesodermal differentiation in the axial region of the gastruloids[24]. There was a posterior-to-anterior signature for somitogenesis with expression of tailbud genes (BRA, CDX2 and LFNG) posteriorly, a short domain of MESP1 and MESP2, followed by a more anterior, broader domain of MEOX1 and TCF15 expression (Fig. 4h). The overall pattern of gene expression therefore mirrors the organisation of paraxial mesoderm specification and differentiation in a mammalian embryo[25], as well as temporal sequences of somitogenesis in hESCs[7,26]. In contrast to these conserved patterns, we also noticed genes that were expressed in different regions (Clusters 0, 2-3 and 13 for example, Supplementary Data 8) or uniquely expressed (Extended Data Fig. 9a-e and Supplementary Data 9) in each of the two systems, supporting the notion that species-specific regulation of patterning might be occurring in the gastruloid models.

Perspectives

The human gastruloid system that we have introduced represents a first step towards the *in vitro* modelling of the emergence of the human body plan in a 3D context. In this regard, the axial organization of the somitogenesis program of gene expression that we observed, suggests an approximate staging. Examination of images of extant collections of human embryos[3] reveals a major transition between Carnegie Stages (CS) 8 and 9 (corresponding to days 17-19 and days 19-21 respectively), associated with the onset of somitogenesis (Fig. 4i); images of CS9 embryos reveal the presence of 1 to 3 somite pairs that are absent in CS8. In the human gastruloids, the pattern of gene expression, with a central somitic domain and posterior presomitic domain of a similar length, leads us to suggests that 72h human

222 gastruloids might serve as a model for some of the features of late CS8 or early CS9 human development. Since, with the current protocol, the majority of human gastruloids curl or retract
224 after 72h, this likely represents a technical limitation, and extension beyond this point will be subject of future studies.

226

The lack of anterior neural and extraembryonic lineages, characteristic of gastruloids, raises
228 important questions about the self-organisation of the mammalian body plan, but also removes several of the ethical considerations associated with prolonged human embryo culture. The
230 tractable nature of human gastruloids should allow the detailed exploration of a variety of questions associated with early human development and represents an experimental model
232 that could prove fruitful in the study of the mechanisms associated with early human development and disease.

References

1 Solnica-Krezel, L. & Sepich, D. S. Gastrulation: making and shaping germ layers. Annu Rev Cell Dev Biol 28, 687-717, doi:10.1146/annurev-cellbio-092910-154043 (2012).

2 Hyun, I., Wilkerson, A. & Johnston, J. Embryology policy: Revisit the 14-day rule. Nature 533, 169-171, doi:10.1038/533169a (2016).

3 O'Rahilly, R., Bossy, J. & Muller, F. Introduction to the study of embryonic stages in man. Bull Assoc Anat (Nancy) 65, 141-236 (1981).

4 Thomson, J. A. et al. Embryonic stem cell lines derived from human blastocysts. Science 282, 1145-1147 (1998).

5 Zhang, X. et al. Pax6 is a human neuroectoderm cell fate determinant. Cell Stem Cell 7, 90-100, doi:10.1016/j.stem.2010.04.017 (2010).

6 Barry, C. et al. Species-specific developmental timing is maintained by pluripotent stem cells ex utero. Dev Biol 423, 101-110, doi:10.1016/j.ydbio.2017.02.002 (2017).

7 Loh, K. M. et al. Mapping the Pairwise Choices Leading from Pluripotency to Human Bone, Heart, and Other Mesoderm Cell Types. Cell 166, 451-467, doi:10.1016/j.cell.2016.06.011 (2016).

8 Warmflash, A., Sorre, B., Etoc, F., Siggia, E. D. & Brivanlou, A. H. A method to recapitulate early embryonic spatial patterning in human embryonic stem cells. Nat Methods 11, 847-854, doi:10.1038/nmeth.3016 (2014).

9 Beccari, L. et al. Multi-axial self-organization properties of mouse embryonic stem cells into gastruloids. Nature 562, 272-276, doi:10.1038/s41586-018-0578-0 (2018).

10 van den Brink, S. C. et al. Symmetry breaking, germ layer specification and axial organisation in aggregates of mouse embryonic stem cells. Development 141, 4231-4242, doi:10.1242/dev.113001 (2014).
11 Davidson, K. C. et al. Wnt/beta-catenin signaling promotes differentiation, not self-renewal, of human embryonic stem cells and is repressed by Oct4. Proc Natl Acad Sci U S A 109, 4485-4490, doi:10.1073/pnas.1118777109 (2012).
12 Allison, T. F. et al. Identification and Single-Cell Functional Characterization of an Endodermally Biased Pluripotent Substate in Human Embryonic Stem Cells. Stem cell reports 10, 1895-1907, doi:10.1016/j.stemcr.2018.04.015 (2018).
13 Martyn, I., Kanno, T. Y., Ruzo, A., Siggia, E. D. & Brivanlou, A. H. Self-organization of a human organizer by combined Wnt and Nodal signalling. Nature 558, 132-135, doi:10.1038/s41586-018-0150-y (2018).
14 Massey, J. et al. Synergy with TGFbeta ligands switches WNT pathway dynamics from transient to sustained during human pluripotent cell differentiation. Proc Natl Acad Sci U S A 116, 4989-4998, doi:10.1073/pnas.1815363116 (2019).
15 Piersma, A. H., Hessel, E. V. & Staal, Y. C. Retinoic acid in developmental toxicology: Teratogen, morphogen and biomarker. Reprod Toxicol 72, 53-61, doi:10.1016/j.reprotox.2017.05.014 (2017).
16 Junker, J. P. et al. Genome-wide RNA Tomography in the zebrafish embryo. Cell 159, 662-675, doi:10.1016/j.cell.2014.09.038 (2014).
17 Wymeersch, F. J. et al. Transcriptionally dynamic progenitor populations organised around a stable niche drive axial patterning. Development 146, doi:10.1242/dev.168161 (2019).
18 Vega-Hernandez, M., Kovacs, A., De Langhe, S. & Ornitz, D. M. FGF10/FGFR2b signaling is essential for cardiac fibroblast development and growth of the myocardium. Development 138, 3331-3340, doi:10.1242/dev.064410 (2011).
19 Watanabe, Y. et al. Fibroblast growth factor 10 gene regulation in the second heart field by Tbx1, Nkx2-5, and Islet1 reveals a genetic switch for down-regulation in the myocardium. Proc Natl Acad Sci U S A 109, 18273-18280, doi:10.1073/pnas.1215360109 (2012).
20 Yoney, A. et al. WNT signaling memory is required for ACTIVIN to function as a morphogen in human gastruloids. Elife 7, doi:10.7554/eLife.38279 (2018).
21 Dunn, N. R., Vincent, S. D., Oxburgh, L., Robertson, E. J. & Bikoff, E. K. Combinatorial activities of Smad2 and Smad3 regulate mesoderm formation and patterning in the mouse embryo. Development 131, 1717-1728, doi:10.1242/dev.01072 (2004).
22 Juan, H. & Hamada, H. Roles of nodal-lefty regulatory loops in embryonic patterning of vertebrates. Genes Cells 6, 923-930 (2001).
23 Kelly, R. G., Buckingham, M. E. & Moorman, A. F. Heart fields and cardiac morphogenesis. Cold Spring Harb Perspect Med 4, doi:10.1101/cshperspect.a015750 (2014).

24 Wilson, V., Olivera-Martinez, I. & Storey, K. G. Stem cells, signals and vertebrate body axis extension. Development 136, 1591-1604, doi:10.1242/dev.021246 (2009).
25 Koch, F. et al. Antagonistic Activities of Sox2 and Brachyury Control the Fate Choice of Neuro-Mesodermal Progenitors. Dev Cell 42, 514-526 e517, doi:10.1016/j.devcel.2017.07.021 (2017).
26 Diaz-Cuadros, M. et al. *In vitro* characterization of the human segmentation clock. Nature, doi:10.1038/s41586-019-1885-9 (2020).

Figure Legends

Fig. 1 | Structure and morphology of human gastruloids. a, Schematic of human gastruloid protocol. Chi, CHIR99021; ROCKi, ROCK inhibitor; E6, Essential 6 medium. **b,** Temporal morphology. Shown are two representative examples from MasterShef7 (mShef7) cell line. (N = 3 experiments). Scalebar, 200 μm. **c,** Estimated number of cells in human gastruloids. Data from 2-4 independent biological replicates (Welch two-sided, two-sample t-test; Source Data). **d,** Elongation of RUES2-GLR gastruloids (center line, median; whiskers, interquartile range). Shown are data from N = 2-4 independent biological replicates (Rep) (Welch two-sided, two-sample t-test; ****, p < 2.2e-16; see Source Data and Methods). **e,** Proportion of elongated RUES2-GLR gastruloids at 72h, as quantified using an automated measure of morphological elongation (see Methods for details). Shown are N = 7 independent biological replicates (left), and the average proportions (right). Representative images of each elongation category can be seen in Extended Data Fig. 1d. **f,** Scanning Electron Micrograph (SEM) of RUES2-GLR human gastruloids at 72h. Shown are two representative examples, n = 28 gastruloids. Scale bars; 200 μm. **g,** Projections of immunofluorescence-labelled RUES2-GLR human gastruloids at 72h (top) and 96h (bottom). Insets, individual sections (bounded by dashed lines). Scale bars; 100 μm. **c-e,** n, number of gastruloids.

Fig. 2 | Dynamic polarization of cell types associated with three germ layers in human gastruloids. a, Schematic of the RUES2-GLR cell line. CDS, Coding Sequence; mCit, mCitrine; tdTom, tdTomato; mCer, mCerulean. **b,** The temporal dynamics of RUES2-GLR human gastruloid development. Shown are two representative examples. Colours indicate reporter fluorescence as in panel (a). Scale bar; 200 μm. Representative example, from N > 5 independent experiments. **c,** Stills from live-imaging of RUES2-GLR human gastruloids. Colours as in panel b. Scale bar; 100 μm. Representative example, from 3 independent experiments. **d,** Localization of the three germ layer reporters at 72h. Shown are 3 examples.

Representative example, from N > 5 independent experiments. Scalebar, 100 μm. **e,** Quantification of the dynamics of reporters along the anteroposterior axis of elongating gastruloids. Thin line, individual gastruloids; thicker line, average of each timepoint. A = Anterior, P = Posterior.

Fig. 3 | Transcriptomic anteroposterior organization of human gastruloids. a, Widefield imaging of 72h RUES2-GLR derived human gastruloids used for tomo-sequencing. Scale bars; 100 μm. mCer, mCerulean; tdTom, tdTomato; mCit, mCitrine. n = 2 gastruloids. **b**, mRNA of the fluorescent reporter transgenes along the anteroposterior (AP) axis. **c,** Transcriptomic analysis of 1,023 significantly reproducible genes along the AP axis of two 72h RUES2-GLR derived Chiron pre-treated human gastruloids. Coloured panels (left) show clusters of genes with similar expression patterns (see Methods, Supplementary Data 1). Two replicates are shown. **d,** Average AP expression for genes in selected clusters, and corresponding enriched Gene Ontology (GO) terms. Shaded ribbon corresponds to the standard deviation of the cluster, line to the mean average (Supplementary Data 3). **e,** Expression of characteristic markers of all three germ layers. Selected genes are highlighted (Supplementary Data 2). Colour-scale equivalent to that of panel (c). **f**, Localisation of HOX gene expression along the AP axis. White bars indicate lack of paralogue. **a-f,** n = 2 gastruloids. See Source Data and Methods.

Fig. 4 | Comparative elements of early embryogenesis. a, Schematic of the mammalian embryo tailbud. **b,** Heatmaps (upper), and line graphs (lower), showing expression localisation of tailbud-associated genes in human gastruloids. Line graphs are displayed as smoothened gene expression patterns; grey ribbon, 50% Confidence Interval. One replicate shown, n = 2 gastruloids; Extended Data Fig. 5c. **c,** Schematic of the mammalian embryo node region. **d,** AP organization of node-associated genes in human gastruloids. Panel organized as in panel c. **e,** Schematic of the mammalian embryo cardiac mesoderm region. **f,** AP organization of cardiac mesoderm region-associated genes in human gastruloids. Panel organized as in panel c. **g,** Heatmap showing AP expression of 253 orthologous, reproducible genes in mouse and human gastruloids (left, average human gastruloid; right, average mouse gastruloid), 20 μm tomo-seq data. Greyscale numbered bars, clustering based on expression patterns; red stars, deviation of expression pattern. n = 2 human gastruloids, 5 mouse gastruloids. **h,** Patterned organization of somitogenesis-related genes in human gastruloids, including signaling gradients (upper heatmaps) and genes related to the tailbud and somitic tissue (lower linegraphs) for n = 2 gastruloids. **i,** Illustration of Carnegie Stage (CS) 8 and 9, showing gross anatomical features, including somite boundaries. Adapted from Ref[32]. Yellow bars,

somites; magenta bars, developing somites and presomitic mesoderm; green bars, primitive streak and tailbud mesoderm; black bars, node. See Source Data and Methods.

Methods

Ethical statement

The human gastruloid model introduced in this study does not show any evidence of cell types associated with anterior neural fates, which would be required to form brain tissue, nor do they form extraembryonic tissues, which would be required for implantation or show evidence of multiorgan differentiation which would be necessary for integrated organ system development. Significantly, they lack the morphology of an early human embryo, and therefore do not manifest human organismal form. As such, they are non-intact, non-autonomous, and non-equivalent to *in vivo* human embryos, and do not have human organismal potential. Our research was subject to review and approval from the Human Biology Research Ethics Committee of the University of Cambridge, in compliance with the ISSCR 2016 guidelines.

Human Cell lines

The cell lines used in this study include the hESC lines: MasterShef7[27], S4-*GATA6*-GFP[12], RUES2-GLR[13] and RUES2:SMAD1-RFP;H2B-mCitrine[20] . All cells were cultured in humidified incubators at 37°C and 5% CO_2. Human ESCs were cultured routinely in Nutristem hPSC XF medium (Biological Industries, 05-100-1A) on 0.5 μg/cm^2 Vitronectin-coated plates (Gibco, A14700). Cells were passaged using 0.5 mM EDTA in PBS$^{-/-}$ (Invitrogen, 15575-038).

Culturing human gastruloids

A critical part of the process is the starting state of the cells, which must be in optimal condition before beginning. When cells were ~40-60% confluent, adherent cultures were pre-treated in Nutristem supplemented with CHIR99021 ('Chiron'; Tocris Biosciences, 4423). We found that cells did not form elongated gastruloids when cultured in alternative pluripotency medium, including mTeSR or Essential8. The optimal concentration of Chiron in this pre-treatment was cell line dependent and was determined empirically by titration for each new line. Concentrations for the lines used in this study are described in the following section. After pre-treatment for 24 hours, cells were dissociated using 0.5 mM EDTA in PBS$^{-/-}$ (Invitrogen, 15575-038), washed in PBS$^{-/-}$ and reaggregated in basal differentiation medium, Essential 6 ('E6'; ThermoFisher, A15165-01), supplemented with 1:2000 Y-27632 ('ROCK inhibitor'; Sigma Aldrich, Y0503) and a cell-line dependent concentration of Chiron. Cell numbers were determined using an automated cell counter (Moxi Z Mini, ORFLO Technologies, MXZ002) and 400-600 cells per 40 μl were added to each well of an ultra-low adherence 96-well plate

(CellStar, 650970). For all images shown here, 400 cells per well of a 96-well plate were used to generate human gastruloids, unless otherwise stated. The cell suspension was centrifuged using a benchtop plate centrifuge at 700 rpm for 2 minutes. The following day, 150 μl fresh E6 medium was added to each well. Medium was exchanged for fresh E6 medium daily following this timepoint. Detailed instructions for generating human gastruloids can be found in Protocol Exchange[28].

Cell line-dependent Chiron pulse

We found that different human ESC lines required different concentrations of Chiron both before aggregation and for the first day of aggregation, in order to generate elongating gastruloids (Extended Data Fig. 1d). Cell-line dependent Chiron doses used in this study were as follows: RUES2-GLR, 3.25 μM Chiron pre-treatment, 0.5 μM Chiron aggregation; MasterShef7, 5 μM Chiron pre-treatment, 3 μM Chiron aggregation; *GATA6*-GFP, 3.25 μM Chiron pre-treatment, 0.5 μM Chiron aggregation; RUES2-SMAD1-RFP;H2B-mCitrine, 5 μM Chiron pre-treatment, 3 μM Chiron aggregation.

Signal Modulation Experiments

RUES2-GLR cells were pre-treated for 1 day in Nutristem supplemented with 100 ng/ml recombinant human Wnt3a (5036-WN-010) or 50 ng/ml BMP4 (314-BP), and aggregated in E6 and ROCK inhibitor with additional supplementation as shown. Subsequent media changes were performed daily with E6 alone. To test the effect of signal modulation on gastruloid formation, RUES2-GLR cells were pre-treated in Nutristem supplemented with 3.25 μM Chiron and one of 1 μM LDN193189 (04-0074), 1 μM XAV-939 (04-0046), or 10 μM SB431542 (1614) before aggregation in E6 with 0.5 μM Chiron and ROCK inhibitor, unless otherwise stated. Subsequent media changes were performed daily with E6 alone. For Retinoic Acid (RA) experiments, RUES2-GLR cells were pre-treated as usual in 3.25 μM Chiron for 1 day, before aggregation in E6 supplemented with 0.5 μM Chiron, ROCK inhibitor and 0.5 μM RA (R2625). Subsequent media changes were performed daily with E6 and 0.5 μM RA.

The SB43 pre-treated gastruloids for tomo-sequencing were made with RUES2-GLR cells pre-treated in Nutristem with 3.25 μM Chiron and 10 μM SB431542 (1614). They were then aggregated in E6 with 3 μM Chiron and ROCK inhibitor. Subsequent media changes were performed daily with E6 alone.

Scanning Electron Microscopy

Human gastruloids, made from the RUES2-GLR line at 72h after aggregation, were washed twice with HEPES buffer and fixed overnight in 3% Glutaraldehyde, 0.05 M sodium cacodylate buffer pH 7.4 at 4°C. Samples were washed several times in de-ionised water (DIW) at room temperature (RT) to remove fixative. Melinex coverslips at 12 mm diameter were covered with a large drop of poly-L-lysine solution (Sigma P4707) and incubated for 15 minutes at RT. Excess solution was drained off and the coverslips were allowed to air-dry at 37ºC. The gastruloids were transferred to the poly-L-lysine coated coverslips in a drop of DIW and allowed to adhere for about 30 min at RT whilst ensuring that the gastruloids remained covered with DIW. Excess DIW was carefully drained off using a tissue paper and the samples were immediately plunge-frozen in liquid nitrogen-cooled ethane. After freeze-drying overnight in a liquid nitrogen-cooled turbo freeze drier (Quorum Emitech K775X), samples were mounted on aluminium SEM stubs using sticky carbon pads and sputter coated with 35 nm Au followed by 15 nm iridium. Samples were viewed in a FEI Verios 460 scanning electron microscope using an Everhart-Thornley detector in secondary electron mode at 2 keV accelerating voltage and 25 pA probe current.

Immunostaining

Human gastruloids were fixed and immunostained according to the existing methods for gastruloid staining[29] unless otherwise stated. The antibodies used were: 1:200 Rabbit anti-CDX2 (ThermoScientific, EPR2764Y); 1:200 Goat anti-GATA6 (R&D Systems, AF1700); 1:200 Rabbit anti-BRACHYURY (AbCam, ab209665); 1:200 Goat anti-SOX2 (R&D Systems, AF2018); 1:200 Mouse anti-CDH2 (BD Biosciences, BD10920); 1:200 Rat anti-CDH1 (Takara, M108), 1:100 Rabbit anti-Wnt3a (ab219412), 1:200 Rabbit anti-LEF1 (ab137872), 1:200 Rabbit anti-FOXA2 (ab108422). All secondary antibodies were all diluted 1:500, and included Alexa-Fluor-488, -568 and -647 conjugated antibodies (Invitrogen).

Adherent cell staining was done using 1:200 Mouse anti-CDH2 (BD Biosciences, BD10920), 1:200 Rat anti-CDH1 (Takara, M108) and 1:200 Rabbit anti-BRACHYURY (AbCam, ab209665) primary antibodies. Quantification was performed using Fiji software on the whole image (histograms) or using a line ROI through the colony (line graph).

In situ *Hybridisation*

Human gastruloids were collected at 72h or 96h post aggregation. After rinsing them briefly in PBS, they were fixed in 4% PFA either overnight or 2h at 4 °C and stored in 100% methanol at −20 °C until further used. *In situ* hybridization was performed on whole mount gastruloids as described[9] with minor modifications. Gastruloids were rehydrated by incubating them for 3-5min in series of decreasing concentration of methanol (75%, 50%, 25% and 0% respectively)

in TBST (20mM Tris 137mM NaCl, 2.7mM KCl, 0.1% Tween, pH = 7,4). After washing gastruloids in TBST, they were incubated in proteinase K (2.5µg/ml) for 2 mins to make them permeable to probes and post-fixed in 4% PFA for 20min at room temperature, before washing again in TBST. To block non-specific interactions, they were prehybridized at 68°C for 4-5 h. Hybridization was performed by incubating them in 200ng/ml of specific digoxigenin (DIG)-labelled RNA probes at 68°C overnight. The probe sequences used can be found in Supplementary Table 2. The following day, after washing the gastruloids at 68°C, they were incubated in blocking solution for 1.5h at solution at room temperature. Gastruloids were then incubated overnight in anti-DIG antibody coupled to alkaline phosphatase (Sigma) at 1:3,000 dilution in blocking buffer at 4°C. The next day, they were washed in MABT (100 mM maleic acid, 150 mM NaCl, 0.1% Tween, pH 7.5) overnight at 4°C. Gastruloids were then washed 3 times with TBST and 3 times in alkaline phosphatase buffer (0.1 M Tris pH 9.5, 100 mM NaCl, 0.1% Tween) and incubated in BM purple solution (Sigma) either at 4°C or RT until the signal was fully developed. Gastruloids were washed in TBST and post fixed in 4% PFA for 20min at RT. For imaging gastruloids were suspended in CUBIC-R1A tissue clearing reagent[30,31].

RT-qPCR

Gene expression was analysed from adherent cells using Trizol (Ambion LifeTechnologies) according to manufacturer's instructions. Total RNA was quantified using a NanoDrop 2000C (ThermoScientific) and 5 μg was added to a reverse transcription reaction with Superscript III (Invitrogen) according to manufacturer's instructions. Resultant cDNA was quantified by qPCR with SYBRGreen (Merck) using a liquid handling robot (Qiagility, Qiagen) and analysed on a RotorGeneQ thermocycler (Qiagen). Primer sequences can be found in Supplementary Table 1. Concentration of cDNA was estimated using an in-house MAK2 analysis method, as described in[32].

Imaging

Confocal imaging was performed using a LSM700 (Zeiss) on a Zeiss Axiovert 200 M using a 40 EC Plan-NeoFluar 1.3 NA DIC oil-immersion objective. Image capture was performed using Zen2010 v6 (Carl Zeiss Microscopy Ltd, Cambridge UK). All samples were fixed and immunostained prior to imaging. For gastruloids made from the RUES2-GLR reporter line, we never observed fluorescent signal of reporter proteins following our fixation protocol, and therefore used the same antibody design and microscope settings as described.

Wide-field imaging was performed using a 37°C incubated chamber supplied with 5% CO_2, attached to a Zeiss AxioObserver.Z1 (Carl Zeiss, UK) as described in[33]. All images were analysed using Fiji software[34], and any adjustments are always consistent within a panel.

Presented images have been rotated to align their AP axis horizontally where necessary, as indicated by a dark grey background.

Image Analysis: Germ Layer Patterning

Human gastruloids made using the RUES2-GLR reporter line were specifically analysed for dynamic reporter expression. An in-house MATLAB script was developed to assess the dynamic fluorescent marker expression along the AP axis of human gastruloids. Widefield images of gastruloids were taken at 24h, 48h and 72h and aligned along their anteroposterior axis with reference to fluorescent reporter expression. For each sample, a binary image was generated in the brightfield channel and used as a mask for all fluorescent channels and the major (length) axis was identified. Consequently, for every pixel along the length axis, the sum of intensity values of the respective channel along the width of the aggregate was divided by the width of the gastruloid at that specific point, yielding the normalized fluorescence intensity along the length of the sample. This process was then repeated for every acquired fluorescent channel. Gastruloids used for this analysis were a full set from one experimental batch, and images were only excluded from the analysis when anteroposterior alignment or binarization were unsuccessful.

Image Analysis: Elongation quantification

In order to quantify the degree of elongation of human gastruloids, brightfield channel widefield images were imported into Fiji[34]. The length of the longest axis was measured using the line tool, followed by the length of the perpendicular axis at the mid-point of the longest axis line. The ratio of these two values was calculated and plotted by time-point and condition, using R. Significance was assessed using the Welch Two-Sample t-test. This method was used to assess the difference in elongation with and without Chiron pre-treatment, as shown in Fig. 1d.

Image Analysis: Morphological quantification

The estimate of the proportions of gastruloid shapes (spherical, ovoid, elongated-short and elongated-long) was estimated for multiple independent biological replicates. This was performed using an in-house method derived from that previously described (Turner 2017, doi: 10.1242/dev.150391). Briefly, images were converted into single-channel, 8-bit TIFF files using FIJI[34]. These were then processed using Python 3.6 (Python Software Foundation, https://www.python.org/) and the Open-CV package[35] to apply a Gaussian blur before performing Otsu's thresholding and floodfilling with erosion to assign a mask around the shape of each gastruloid. The length and width values were calculated using a rotated bounding box (minAreaRect), which identifies and measures the orthogonally widest and longest parts of

the gastruloid. Various additional quantitative features were then extracted from the contours, which were further processed using R. The categories of each shape descriptor were defined as follows: Spherical, Circularity less than or equal to 1.1 or Max Width : Max Length (WL) greater than or equal to 0.95; Ovoid, Circularity less than or equal to 1.2 or WL greater than or equal to 0.9; Elongated – Short, Circularity greater than 1.2 and less than or equal to 1.4 and WL less than 0.9; Elongated – Long, Circularity less than 1.4 and WL less than 0.9. Images were quality controlled for empty wells or those with debris that compromised shape descriptors, using quantification of area or circularity outliers and confirmed manually by examination of images. This method was used to assess the reproducibility of human gastruloid experiments, as shown in Fig. 1e and Extended Data Fig. 1d.

Image Analysis: Estimates of cell number

The number of cells per aggregate was estimated using Imaris software (Bitplane) on confocal images stained with Hoechst. Spots were drawn using the internal algorithm, using an estimated xy size of 6 μm, a quality threshold of 2.5 and background subtraction. Because the light penetration only allowed us to image part of the gastruloid we assumed this was on average half of the gastruloid, and so doubled the resultant nuclei estimate. It is likely that this process slightly underestimates the number of nuclei. The quantitative data were subsequently analysed in R. The fitting of an exponential curve was done using the lm() function of log transformed data.

Image Analysis: Subcellular localisation of SMAD1-RFP

To quantify the level of active SMAD1 in each cell of the gastruloid, we sought to determine the nuclear to cytoplasmic ratio of SMAD1-RFP. To do this, we used Imaris software to identify nuclear positions by creating a surface using the Hoechst channel. We then used these surfaces to create two masks: one where everything inside the nuclear mask was set to zero, and one where everything outside the nuclear mask was set to zero. This allowed us to distinguish the nuclear and cytoplasmic components of the SMAD1-RFP signal. To assign the cytoplasmic component to each individual cell, we used Imaris to create Spots using the Hoechst channel (estimated xy diameter: 5.25 μm). These were then processed using 'Spots to Spots Nearest Neighbour Distance' to create maximal cell areas relative to their neighbours. We then used these distance-spots to assess the internal nuclear and cytoplasmic component of SMAD1-RFP in each cell along the AP axis.

The data was subsequently analysed in R, by normalising the mean intensity of the nuclear SMAD1-RFP component to the mean intensity of the H2B-mCitrine value, in order to account

for depth bias. This normalised SMAD1-RFP intensity was then divided by the mean intensity of the cytoplasmic SMAD1-RFP, to get the normalised nuclear : cytoplasmic SMAD1-RFP values.

Image Analysis: Axial patterning quantification

RUES2-GLR gastruloids were fixed at 24, 48 and 72h timepoints, stained for GATA6 and CDX2, and imaged on a confocal. Maximal projection images were generated using Imaris software, and nuclei were identified with Imaris using Hoechst staining (estimated xy size of 6 μm, and quality threshold of 2.5). For each nuclear spot, the mean intensity of GATA6 and CDX2 fluorescence was acquired and plotted using R. Axial patterning was determined in Fiji using the segmented line tool with width 80 and the plotprofile tool. For each gastruloid, the AP axis was normalised between 0 and 1, and the fluorescent intensities were also scaled between 0 and 1 for the minimum and maximum values, in order to aid comparison between gastruloids. The Aspect Ratio of these gastruloids was calculated manually in Fiji using the line tool, where the length of the perpendicular axis at the mid-point of the longest axis line was defined as the width. Three categories, with cut-offs of < 2.0, > 2.0 and < 2.4, and > 2.4, corresponded to the observed longest elongation at 24, 48 and 72 hours, respectively. This method was used for quantifying elongation in confocal images, as shown in Extended Data Fig. 3e-f.

Tomo-sequencing and Mapping

Tomo-sequencing was performed using an updated version of published methods[16,36] and analysed with methods described in van den Brink *et. al*. (associated manuscript). Briefly, gastruloids were sectioned along their AP axis, and the mRNA-content of each section was extracted using SORT-seq[37]. Paired end (75 bp) sequencing was performed on the resulting RNA-seq libraries using the Illumina Next-Seq sequencing platform. Read 1 contains the section barcode and the unique molecular identifier (UMI). Read 2 contains the biological information. Reads 2 with a valid cell/section barcode were selected and mapped using STAR-2.5.3a with default parameters to the human GRCh38 genome (ENSEMBL version 93), and only reads mapping to gene bodies (exons or introns) were used for downstream analysis. Reads mapping simultaneously to an exon and to an intron were assigned to the exon. Mappabilities for the different samples range between 44% and 47%. For each section, the number of transcripts was obtained as previously described[38]. We refer to transcripts as unique molecules based on UMI correction.

After mapping, spike-ins, ribosomal, and mitochondrial genes were removed from downstream analysis, together with *KCNQ1OT1*, *LARS2*, and *MALAT1*, because these genes seem to be linked to mapping errors and have been shown to be erroneous in earlier studies.
In each gastruloid, data was then normalized to the median number of unique transcripts per slice, and the z-score of each gene was extracted along sections.

Gene Expression Data Analysis

The reproducibility of AP expression pattern between different gastruloid replicates was scored for each gene using a random background model to calculate the Pearson correlation coefficient p-value (see ref 39 for further details). The p-value threshold to select reproducible genes was set at 0.001. These significantly reproducible genes were then clustered using a Self-Organising Map (SOM) method, followed by Hierarchical Clustering to determine general patterns of gene expression along the AP axis.

Average gastruloid profiles were generated using the mean of z-scores along the AP axis. When the number of sections between replicates was different, values were quadratically interpolated to fill spaces using the **interp1d** function from the package **scipy.interpolate** (Python 3.6).

Differential gene expression was performed by normalizing the transcripts in each section to 100,000 for all gastruloids; then pooling all sections of each gastruloid together; and finally assessing significant differentially expressed genes based on total expression using the Binomial test.

For smoothened line-graphs of gene expression, the distribution of gene expression along the sections was plotted using R, and smoothened using the geom_smooth() function (method = loess, span = 0.3, level = 0.5) to minimise background variability. For each gene expression distribution, the confidence interval is therefore shown (at 0.5 Confidence Interval) as a grey ribbon.

Gene Ontology (GO) term analysis for each hierarchical cluster of the Chiron pre-treated human gastruloids was performed using ENSEMBL IDs run with the DAVID Annotation tool[40] with the human genome as a background model, focussing on Biological Process terms. Statistical correction for multiple comparisons was achieved using Benjamini adjustment.

Gene Ontology for each hierarchical cluster of the human-to-mouse gastruloid comparison was performed using the python package goatools[41], which uses Fishers exact test, setting

the p-value at 0.05. Both the list of reproducible genes in each corresponding condition, or the full human transcriptome was set as a background model, focussing on Biological Process terms. Statistical correction for multiple comparisons was achieved using Bonferroni adjustment.

Mouse Gastruloid comparison

We compared 72h human gastruloids, which we believe correspond approximately to the ~CS9 human embryo, with 120h mouse gastruloids which are thought to represent an ~E8.0-E8.5 stage embryo and approximately equivalent developmental stages of both species[40]. These mouse gastruloids were generated from the LfngT2AVenus line[42]. Full details of this dataset can be found in ref 39.

Gene reproducibility analysis between the replicates of mouse gastruloids (P-value < 0.01) and the 2 replicates of human gastruloids (P-value < 0.001) was performed, independently (as described above). Only genes present in the two separate lists that had human-mouse orthologs were used for downstream analysis. The list of human-mouse orthologs was obtained from Biomart, Ensembl 93. Genes were clustered based on their AP expression pattern in both the mouse and the human average gastruloid simultaneously, as described above. The Pearson correlation coefficient for each gene was calculated between the AP expression pattern of two different samples (in z- score units). To assess for significantly correlated genes, we randomly generated 10,000 expression profiles with the same number of sections as in the pair of replicates and determine the correlation value at which less than 100 random profiles have larger correlation values (P-value < 0.01).

References

27 Canham, M. A. et al. The Molecular Karyotype of 25 Clinical-Grade Human Embryonic Stem Cell Lines. Sci Rep 5, 17258, doi:10.1038/srep17258 (2015).

28 Moris, N. et al. Generating Human Gastruloids from Human Embryonic Stem Cells. . Protocol Exchange doi: 10.21203/rs.2.21540/v1 (2020).

29 Baillie--Johnson, P., van den Brink, S., Balayo, T., Turner, D. A. & Martinez Arias, A. Generation of aggregates of mouse ES cells that show symmetry breaking, polarisation and emergent collective behaviour. JOVE doi: 10.3791/53252 (2014).

30 Susaki, E. A. et al. Whole-brain imaging with single-cell resolution using chemical cocktails and computational analysis. Cell 157, 726-739, doi:10.1016/j.cell.2014.03.042 (2014).

31 Susaki, E. A. et al. Advanced CUBIC protocols for whole-brain and whole-body clearing and imaging. Nat Protoc 10, 1709-1727, doi:10.1038/nprot.2015.085 (2015).

32 Turner, D. A. et al. Wnt/beta-catenin and FGF signalling direct the specification and maintenance of a neuromesodermal axial progenitor in ensembles of mouse embryonic stem cells. Development 141, 4243-4253, doi:10.1242/dev.112979 (2014).

33 Turner, D. A. et al. Anteroposterior polarity and elongation in the absence of extra-embryonic tissues and of spatially localised signalling in gastruloids: mammalian embryonic organoids. Development 144, 3894-3906, doi:10.1242/dev.150391 (2017).

34 Schindelin, J. et al. Fiji: an open-source platform for biological-image analysis. Nat Methods 9, 676-682, doi:10.1038/nmeth.2019 (2012).

35 Bradski, G. The OpenCV library. Journal of Software Tools Dr. Dobb's (2000).

36 Kruse, F., Junker, J. P., van Oudenaarden, A. & Bakkers, J. Tomo-seq: A method to obtain genome-wide expression data with spatial resolution. Methods Cell Biol 135, 299-307, doi:10.1016/bs.mcb.2016.01.006 (2016).

37 Muraro, M. J. et al. A Single-Cell Transcriptome Atlas of the Human Pancreas. Cell Syst 3, 385-394 e383, doi:10.1016/j.cels.2016.09.002 (2016).

562 38. Grün, D., Kester, L. & van Oudenaarden, A. Validation of noise models for single-cell transcriptomics. *Nat. Methods* **11,** 637–640 (2014). doi: 10.1038/nmeth.2930 39

564

39 van den Brink, S. et al. **Single-cell and spatial transcriptomics reveal somitogenesis in gastruloids**. Nature In press (2020)

40. Huang da, W., Sherman, B. T. & Lempicki, R. A. Systematic and integrative analysis of large gene lists using DAVID bioinformatics resources. Nat Protoc 4, 44-57, doi:10.1038/nprot.2008.211 (2009).

41 Klopfenstein, D. V. et al. GOATOOLS: A Python library for Gene Ontology analyses. Sci Rep 8, 10872, doi:10.1038/s41598-018-28948-z (2018).

42 Theiler, K. The house mouse: Atlas of embryonic development. 2nd edn, (Springer Verlag 1989).

Acknowledgements

566 We thank V. Trivedi for his help writing the dynamic fluorescent reporter analysis code, D. Turner and A. Baranowski for their help developing the image analysis code, K. Muller from 568 the Cambridge Advance Imaging Centre (CAIC) for help with Scanning Electron Microscopy, the Utrecht Sequencing facility for sequencing and A. Ebbing, J. Vivié and M. Betist for the 570 robotized tomo-seq protocol. We also wish to thank members of the Martinez Arias and van Oudenaarden laboratories, as well as B. Steventon, P. Rugg-Gunn, M. Lütolf, M. Johnson and 572 N. Hopwood for discussions over the course of this work. This work was supported by funds from the Newton Trust (INT16.24b), Leverhulme Trust (RPG-2018-356) and MRC 574 (MR/R017190/1) to A.M.A., and a European Research Council Advanced grant (ERC-AdG 742225-IntScOmics), a Nederlandse Organisatie voor Wetenschappelijk Onderzoek (NWO)

TOP award (NWO-CW 714.016.001), and the Foundation for Fundamental Research on Matter, financially supported by NWO (FOM-14NOISE01) to S.C.v.d.B., A.A. and A.v.O.. This work is part of the Oncode Institute which is partly financed by the Dutch Cancer Society. It was also supported by a Constance Work Junior Research Fellowship from Newnham College, Cambridge to N.M. and an Erasmus+ grant to K.A..

Author Contributions

N.M. and K.A. designed, optimised and performed the human gastruloid experiments, with help from T.B. and A.M.A, and the A.v.O. lab replicated the entire process, independently. N.M. and S.v.d.B. embedded the human gastruloids, and S.v.d.B. performed sectioning and tomo-sequencing preparation. A.A. analysed transcriptomic datasets, with analysis input from N.M., S.v.d.B., A.v.O. and A.M.A.. N.M. created embryonic illustrations. J.S. designed and made *in situ* probes, and J.S. and S.G. performed in situ hybridisations. A.M.A. and A.v.O. supervised research. N.M and A.M.A. wrote the manuscript with considerable input from all authors. All authors reviewed the manuscript.

Author Information

Naomi Moris, Kerim Anlas, Susanne van den Brink and Anna Alemany contributed equally to this work.

Competing Interests

This work is the subject of a patent application (PCT/GB2019/052670) filed by Cambridge Enterprise on behalf of the University of Cambridge, covering the generation and use of human gastruloids. The inventors are NM and AMA. The rest of the authors declare no competing interests.

Correspondence

Correspondence to Naomi Moris (nem33@cam.ac.uk), Alfonso Martinez Arias (ama11@cam.ac.uk) and Alexander van Oudenaarden (a.vanoudenaarden@hubrecht.eu).

Data Availability Statement

All RNA-seq datasets produced in this study are deposited in the Gene Expression Omnibus (GEO) under accession code GSE123187. Source data for Figures 1-4 and Extended Data Figures 1-9 are provided within the manuscript files.

Code Availability Statement

Code is available upon request to the authors.

608 **Extended data**

Nine Extended Data Figures, nine Supplementary Data files, three Supplementary Videos and
610 two Supplementary Tables are available for this paper.

Extended Data Fig. 1 | Chiron pre-treatment optimisation and Morphological variability. **a,** Aggregation of single RUES2-GLR cells following Chiron pre-treatment, showing either a single aggregate (left) or presence of transient 'satellite' aggregates (right). These typically merge within 10 hours (n = 38 gastruloids from N = 2 experiments). **b,** Schematic of protocol without Chiron pre-treatment, but with aggregation in Chiron (Chi) and ROCK inhibitor (ROCKi) medium. **c,** Gastruloids made from the RUES2-GLR line without Chiron pre-treatment at 24, 48 and 72h after aggregation. Shown are 3 representative examples for each timepoint (n = 415 gastruloids), with all three fluorescent reporters (SOX2-mCitrine, SOX17-tdTomato and BRA-mCerulean; left) and without SOX2-mCitrine (right). Scalebar; 100 μm. Representative example, from N = 5 independent experiments. **d,** Examples of reporter patterning in differential morphology classes, as assessed by automated segmentation providing gastruloid outline boundaries (yellow line indicates boundary used for quantifications). Three representative gastruloids per category are shown (n = 374 gastruloids). See methods for details of classification method. Scale bar, 100 μm. Representative examples, from N = 7 independent experiments. **e,** Cell line-dependent optimisation of Chiron conditions. Shown are MasterShef7 cell-derived human gastruloids (left; two examples shown) or RUES2-GLR cell-derived human gastruloids (right; three examples are shown). Scalebars; 100 μm. Red bounding boxes indicate concentrations at which gastruloids were deemed to be optimally elongated, and resultant conditions for subsequent gastruloid derivation. Representative examples, from N = 3 independent experiments.

Extended Data Fig. 2 | Effect of Chiron pre-treatment on human embryonic stem cells. **a,** Gene expression following 24 hours of Chiron pre-treatment (Chi PT) in adherent RUES2-
612 GLR cells compared to non-pretreated cells (No PT) in Nutristem alone, as assessed by RT-qPCR. Shown are averages from 5 biological replicates; bars, mean average; points, technical
614 averages for each experimental replicate. Significance (ns, $p > 0.05$, *, $p < 0.05$; **, $p < 0.01$; ***, $p < 0.001$; Welch two-sided, two-sample t-test; Source Data and Methods). **b,**
616 Immunostaining of adherent colonies of RUES2-GLR cells for BRACHYURY, E-CADHERIN and N-CADHERIN (CDH1 and CDH2 respectively) with non-pretreated cells (top) or following
618 24h Chiron (Chi) pre-treatment (bottom). Scalebar; 100 μm. Dotted region on colony (top

panels) shows position of enlarged region (bottom panels). Representative example, from N = 2 independent experiments. **c,** Quantified expression from immunostaining of RUES2-GLR cells, as shown in panel b. The whole image was used to generate this data. **d,** Profiles of membrane localisation of E- and N-cadherin from immunostaining of RUES2-GLR cell colonies, as shown in panel b.

Extended Data Fig. 3 | Establishing axial patterning in human gastruloids. a, Immunofluorescence imaging of a RUES2-GLR human gastruloid at 24h. Shown are confocal sections (top) and mean projection (bottom) of the gastruloid. Scalebar; 100 μm. Representative example from n = 12 gastruloids, from N = 2 experiments. **b,** Human gastruloids made from MasterShef7 cell line at 72 hours after aggregation, showing BRA, SOX2 and N-Cadherin (CDH2) localisation. Shown are 3 representative examples. Scalebar; 100 μm. Representative example from n = 13 gastruloids, from N = 3 experiments. **c,** Projection of immunofluorescently labelled RUES2-GLR derived human gastruloids at 24, 48 and 72h with GATA6 (magenta) and CDX2 (yellow) staining. Shown are 6 representative gastruloids at each timepoint. Scalebar, 30 μm; small text, Aspect Ratio. Representative examples from n = 63 gastruloids from N = 2 independent experiments. **d,** Scatterplot of co-expression of GATA6 and CDX2 per cell, across the three timepoints. Blue points, co-expression over threshold; Grey points, expression below threshold; Small text, number of gastruloids in each plot (n). **e,** Relative axial expression of GATA6 (magenta) and CDX2 (yellow) along the AP axis. Small text, number of gastruloids in each plot (n). **f,** Relative axial expression of GATA6 (magenta) and CDX2 (yellow) along the AP axis, as stratified by aspect ratio (as determined using a manual axial patterning quantification, see Methods for details). Small text, number of gastruloids in each plot (n). Thick lines, mean average; Thin lines, individual gastruloids. Representative images of such gastruloid elongation classifications can be seen in panel c. **g,** Progressive polarisation and restriction of GATA6-GFP fluorescence to the anterior pole of human gastruloids made from the S4-GATA6-GFP cell line. Scalebar; 100 μm. Representative example from n = 17 gastruloids.

Extended Data Fig. 4 | Disrupting axial patterning in human gastruloids. a, Aggregates following pre-treatment with Wnt3a instead of Chiron for 24h in RUES2-GLR cells. Representative examples shown (n = 281 gastruloids). **b,** Aggregates following pre-treatment with BMP4 for 24h in RUES2-GLR cells. Representative examples shown (n = 187 gastruloids). **c,** Application of a BMP inhibitor, LDN193189 (LDN; left) or Tankyrase inhibitor, XAV-939 (XAV; right) during 24h pre-treatment of RUES2-GLR cells. Representative examples shown (n = 85 gastruloids). **d,** Application of a Nodal signalling inhibitor, SB43

(SB43) during 24h pre-treatment of RUES2-GLR cells. **a-d,** Representative examples from N = 3 independent experiments. Dark green bounding box indicates the pre-treatment condition in Nutristem, and teal box indicates the aggregation medium composition in E6 and ROCK inhibitor. Shown are 2 representative examples from each condition. Scalebar; 100 μm. **e,** Addition of Retinoid Acid (RA, right) or DMSO (left) on RUES2-GLR derived human gastruloids for each day of aggregate development. Schematic of protocol (top) and imaging results (bottom). See Methods for experimental details. Scale bar; 100 μm. Representative examples of n = 159 gastruloids, from N = 4 independent experiments. **f,** Confocal imaging of axial patterning defects in RA-treated 72h RUES2-GLR derived human gastruloids. Scalebar; 100 μm. Representative examples of n = 25 gastruloids, from N = 3 independent experiments.

Extended Data Fig. 5 | Spatial transcriptomics by tomo-seq identifies clusters of gene expression. a, Quantification of number of genes (left) and number of unique transcripts (right) detectable in each section along the anterior-posterior (AP) axis of 72h Chiron pre-treated human gastruloids made from RUES2-GLR cells. Blue bars, sections above the threshold used for downstream tomo-seq analysis; Grey bars, sections below the threshold (see Methods for details). Two replicates are shown. **b,** Average expression patterns along the AP axis of all genes detected in each cluster. Clusters correspond to those in Fig. 3b and Supplementary Data 1. Ribbon indicates standard deviation for the set of genes within each cluster, line to the mean average. n = 2 gastruloids. **c,** Selection of gene traces along the AP axis for both gastruloids. Blue and green lines, expression values for replicate 1 and 2 respectively.

Extended Data Fig. 6 | Transcriptional profiles and anterio-posterior (AP) localisation in human gastruloids. a, Normalised expression of anterior neural genes in human gastruloids. **b,** Total expression (log10 transformed) of each HOX gene across all sections of Gastruloid 1 (upper) and Gastruloid 2 (lower), for all 4 clusters (HOXA, HOXB, HOXC and HOXD). White boxes indicate that a gene is not present in the human genome. **a-b,** n = 2 gastruloids. **c,** Expression of FOXA2 in the posterior end of 72h Chiron pre-treated RUES2-GLR gastruloids. Three representative examples are shown (n = 8 gastruloids). **d,** Expression of ligands of the BMP (top) and WNT (bottom) signalling pathways. Red box indicates genes with particularly strong AP localisation bias, n = 2 gastruloids. **e,** Maximum projection confocal images of human gastruloids at 72h made from the SMAD1-RFP;H2B-mCitrine cell line. Three representative examples are shown. Inset, close-up of region shown in red dashed-line bounded boxes. Scalebar; 40-50 μm (indicated on image). Representative examples of n = 19 gastruloids, from N = 2 independent experiments. **f,** Processing to separate nuclear and

cytoplasmic component of SMAD1-RFP signal (left; see Methods for details) and resultant quantification of normalised nuclear : cytoplasmic ratio of SMAD1-RFP along the AP axis (right; each point represents a cell). Three representative examples are shown. Representative examples from N = 2 independent experiments. Scale bar as in panel e. **g,** Immunostaining of LEF1 and BRA expression in 96h RUES2-GLR human gastruloids. LEF1 is localised in a gradient primarily in the posterior portion of the gastruloids. Scalebar; 100 μm. Shown are two representative examples, of n = 10 gastruloids, from N = 3 independent experiments. **h,** Immunostaining of WNT3A and BRA expression in 72h RUES2-GLR human gastruloids, showing close-up of posterior end. Scalebar; 50 μm. Max Proj; Maximum Projection. Shown is one representative example from n = 8 gastruloids, N = 2 independent experiments. **i,** Localised expression of Nodal signalling-related genes towards the posterior of Chiron pre-treated human gastruloids by tomo-sequencing, n = 2 gastruloids.

Extended Data Fig. 7 | Perturbation of Nodal signaling in human gastruloids. a, Schematic representation of the protocol used to generate Chiron (Chi) and SB431542 (SB43) pre-treated human gastruloids (Chi + SB43). See Methods for details. **b,** Representative examples of the dynamic development of Chi + SB43 pre-treated gastruloids, from RUES2-GLR cells (N = 3 experiments). Colours indicate reporter fluorescence as indicated in Fig. 2a. Scale bar, 100 μm. **c,** *In situ* hybridisation against *BRA* and *SOX2* mRNA in 96h Chi + SB43 gastruloids. Four representative examples are shown for each gene. **d,** Widefield imaging of the two 120h RUES2-GLR derived Chi + SB43 pre-treated human gastruloids used for tomo-sequencing. Scale bars; 100 μm. mCer, mCerulean; tdTom, tdTomato; mCit, mCitrine. **e,** Venn diagram showing number of reproducibly-localised genes in the Chiron pre-treated human gastruloids (Chi hGld; green) and in the Chiron and SB43 pre-treated human gastruloids (Chi + SB43 hGld; yellow). Numbers indicate counts of genes and percentage values in brackets indicate proportion of the full figure. See Source Data. **f,** Differentially expressed genes between Chi and Chi + SB43 pre-treated gastruloids (total expression). See Source Data and Supplementary Data 6 and Methods. **g,** Gene expression patterns detected in an averaged Chi pre-treated and averaged Chi + SB43 pre-treated gastruloid. Grey/Black panels show the hierarchical clustering of gene expression; Blue/Red bands indicate selective reproducibility between replicates from one or other pre-treatment conditions (Red, Chi + SB43 only; Blue, Chi only; Grey; both); Dark red box, cluster for which expression is lost following SB43 pre-treatment (Cluster 4); White rows, lack of expression detected. See Methods for details. See Source Data and Supplementary Data 4. **a-g,** n = 2 Chi and 2 Chi + SB43 gastruloids.

Extended Data Fig. 8 | Transcriptional profiles of gastruloids exposed to Nodal inhibition before aggregation. a, Quantification of number of genes (left) and number of unique transcripts (right) detectable in each section along the anterior-posterior (AP) axis of Chiron + SB43 pre-treated human gastruloids made from 120 h RUES2-GLR gastruloids. Blue bars, sections above the threshold used for downstream tomo-seq analysis; Grey bars, sections below the threshold (see Methods for details). Two replicates are shown. **b,** Significantly reproducible gene expression patterns of individual replicates of Chiron + SB43 pre-treated human gastruloids (left), and resultant average gastruloid (right) along the AP axis. See Source Data and Supplementary Data 4. **c,** Average expression pattern of genes from each cluster shown in panel (b). Ribbon indicates standard deviation for the set of genes within each cluster, line to the mean average. **d,** Expression detected for markers of all three germ layers. White rows indicate lack of expression detected for that gene. See Source Data and Supplementary Data 7. **e,** Gene expression traces along the AP axis of the four human gastruloids (gray lines, Chiron pre-treatment; blue lines, Chi + SB43 pre-treatment; solid lines, Replicate 1; dashed lines, Replicate 2). **a-e,** n = 2 gastruloids.

Extended Data Fig. 9 | Unique transcriptional profiles of mouse and human gastruloids. a, Venn diagram showing number of common reproducibly localised genes in the Chiron pre-treated human gastruloids (Chi hGld; green), the Chiron and SB43 pre-treated human gastruloids (Chi + SB43 hGld; yellow) and the mouse gastruloids (mGld; blue). Numbers indicate counts of genes and percentage values in brackets indicate proportion of the full figure. **b,** Unique reproducibly-localised gene expression in mouse gastruloids, not detected in Chiron pre-treated human gastruloids. **c,** Unique reproducibly localised gene expression in Chiron pre-treated human gastruloids, not detected in mouse gastruloids. **d,** Genes reproducibly localised in mouse gastruloids and expressed, but not reproducibly localized, in Chiron pre-treated human gastruloids. **e,** Genes reproducibly-localised in Chiron pre-treated human gastruloids and expressed, but not reproducibly localized, in mouse gastruloids. See Source Data and Supplementary Data 9. **a-e,** n = 2 human gastruloids, 3 mouse gastruloids.

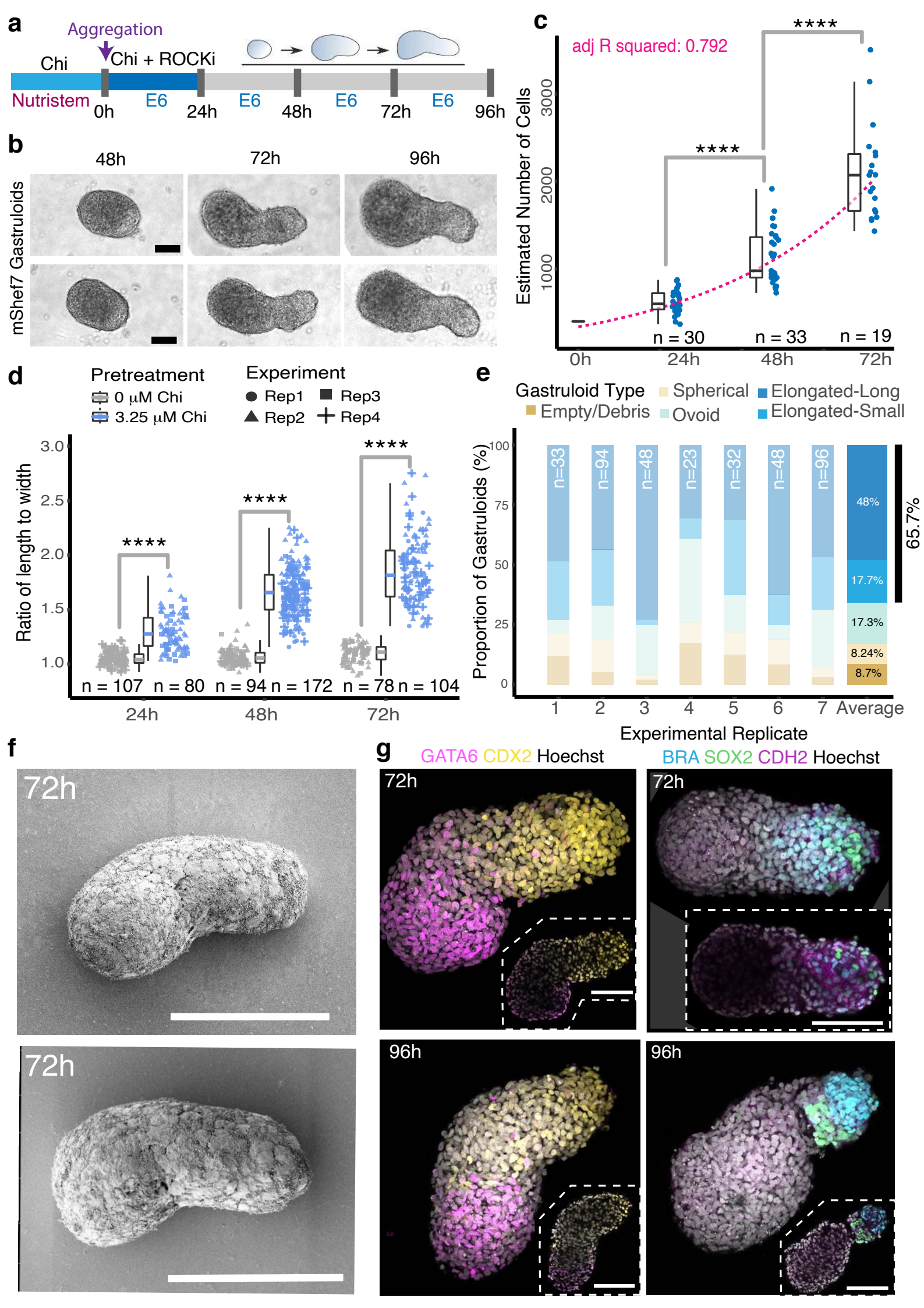
a
Aggregation
Chi
Chi + ROCKi
Nutristem
E6
0h
24h
48h
72h
96h
b
48h
72h
96h
mShef7 Gastruloids
c
adj R squared: 0.792
****
Estimated Number of Cells
1000
2000
3000
n = 30
n = 33
n = 19
0h
24h
48h
72h
d
Pretreatment
0 μM Chi
3.25 μM Chi
Experiment
Rep1
Rep2
Rep3
Rep4
Ratio of length to width
n = 107
n = 80
n = 94
n = 172
n = 78
n = 104
24h
48h
72h
e
Gastruloid Type
Spherical
Elongated-Long
Empty/Debris
Ovoid
Elongated-Small
Proportion of Gastruloids (%)
n=33
n=94
n=48
n=23
n=32
n=48
n=96
48%
17.7%
17.3%
8.24%
8.7%
65.7%
Average
Experimental Replicate
f
72h
72h
g
GATA6 CDX2 Hoechst
BRA SOX2 CDH2 Hoechst
72h
72h
96h
96h

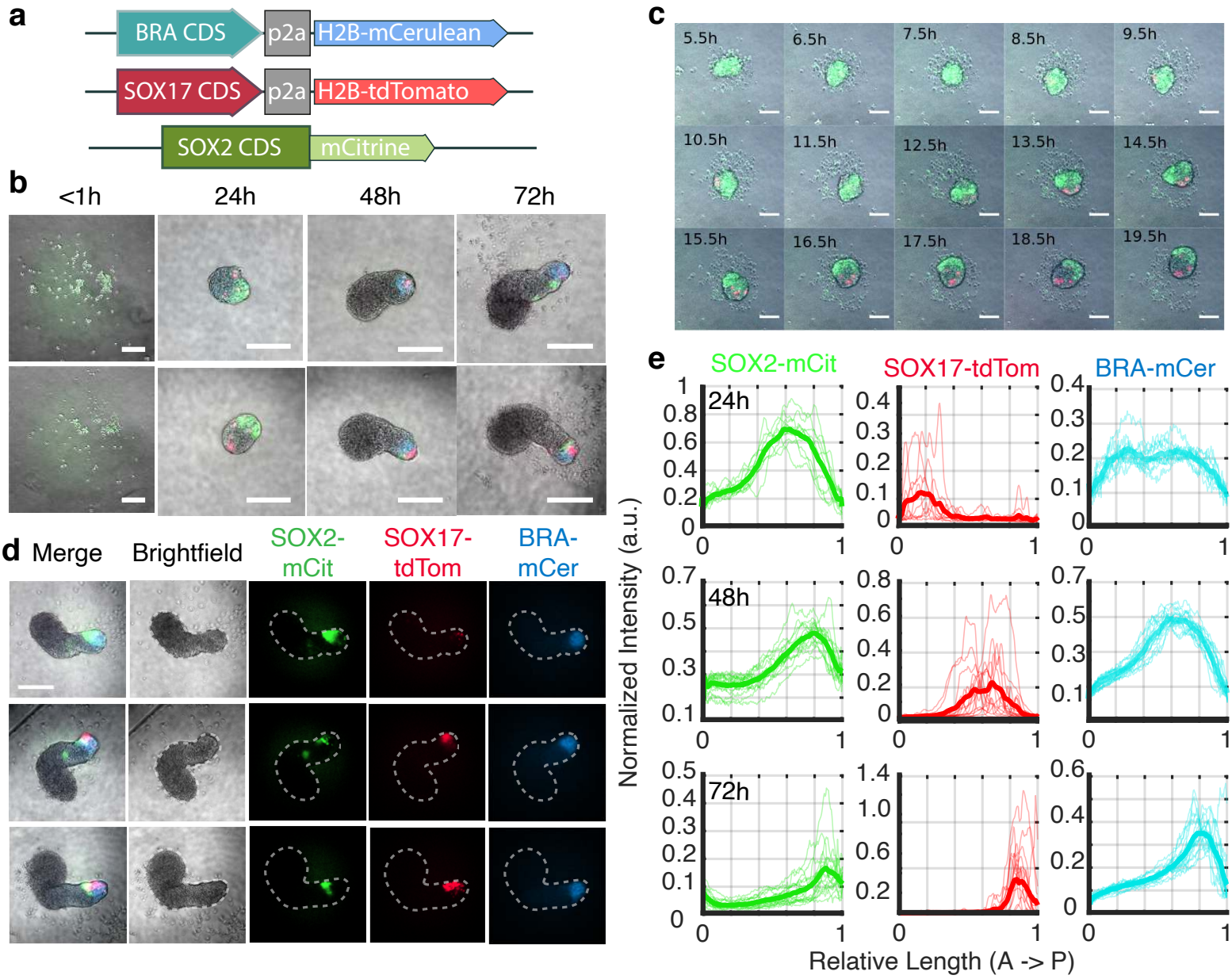
a
BRA CDS
p2a
H2B-mCerulean
SOX17 CDS
p2a
H2B-tdTomato
SOX2 CDS
mCitrine
b
<1h
24h
48h
72h
c
5.5h
6.5h
7.5h
8.5h
9.5h
10.5h
11.5h
12.5h
13.5h
14.5h
15.5h
16.5h
17.5h
18.5h
19.5h
d
Merge
Brightfield
SOX2-mCit
SOX17-tdTom
BRA-mCer
e
SOX2-mCit
SOX17-tdTom
BRA-mCer
24h
48h
72h
Normalized Intensity (a.u.)
Relative Length (A -> P)

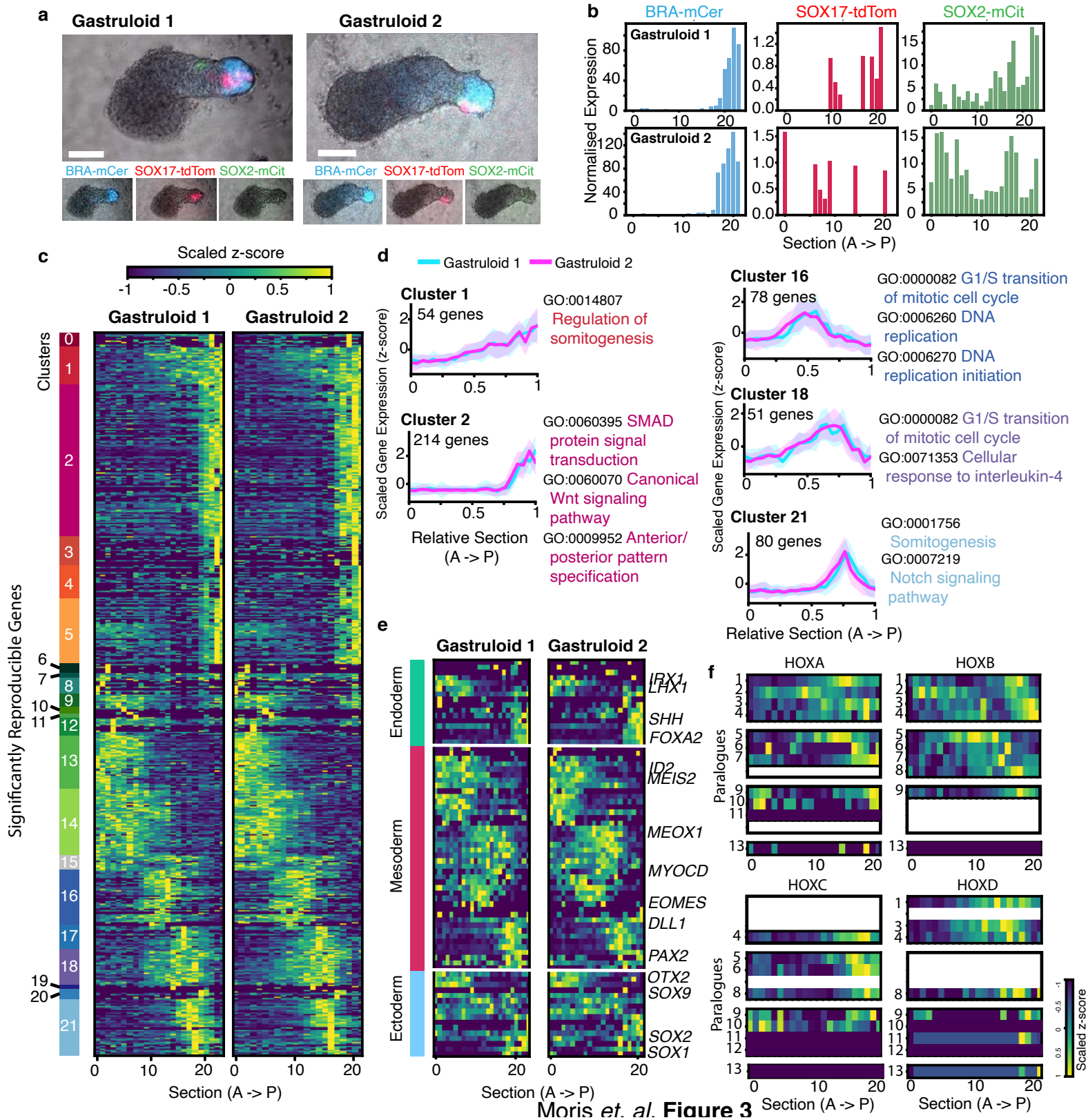

Moris *et. al.* **Figure 3**

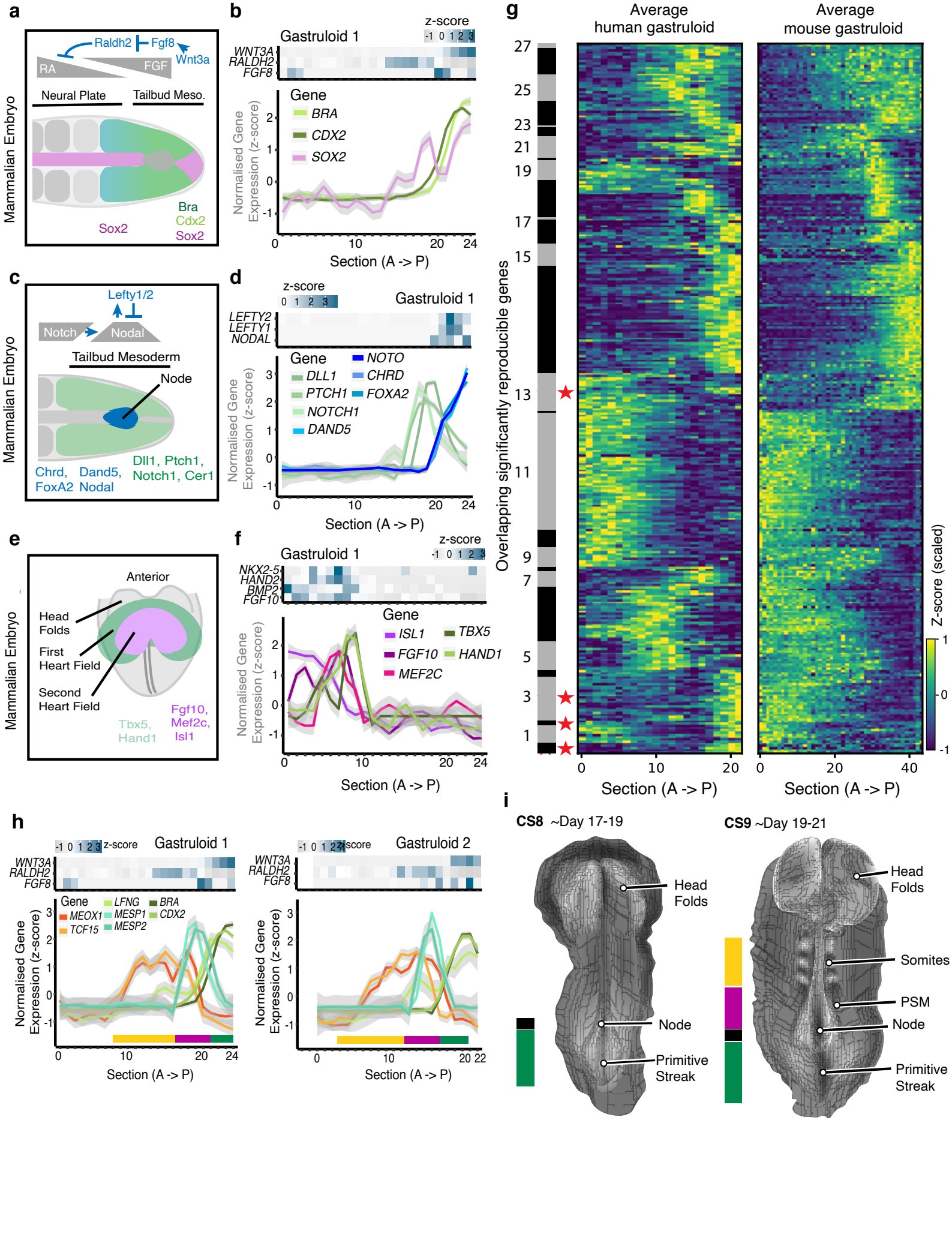
a
Mammalian Embryo
Raldh2
Fgf8
Wnt3a
RA
FGF
Neural Plate
Tailbud Meso.
Bra
Cdx2
Sox2
Sox2
b
Gastruloid 1
z-score
-1 0 1 2 3
WNT3A
RALDH2
FGF8
Gene
BRA
CDX2
SOX2
Normalised Gene Expression (z-score)
Section (A -> P)
c
Mammalian Embryo
Lefty1/2
Notch
Nodal
Tailbud Mesoderm
Node
Chrd, FoxA2
Dand5, Nodal
Dll1, Ptch1, Notch1, Cer1
d
z-score
Gastruloid 1
LEFTY2
LEFTY1
NODAL
Gene
NOTO
CHRD
DLL1
FOXA2
PTCH1
NOTCH1
DAND5
Normalised Gene Expression (z-score)
Section (A -> P)
e
Mammalian Embryo
Anterior
Head Folds
First Heart Field
Second Heart Field
Tbx5, Hand1
Fgf10, Mef2c, Isl1
f
Gastruloid 1
z-score
NKX2-5
HAND2
BMP2
FGF10
Gene
ISL1
TBX5
FGF10
HAND1
MEF2C
Normalised Gene Expression (z-score)
Section (A -> P)
g
Average human gastruloid
Average mouse gastruloid
Overlapping significantly reproducible genes
Z-score (scaled)
Section (A -> P)
Section (A -> P)
h
Gastruloid 1
Gastruloid 2
z-score
WNT3A
RALDH2
FGF8
Gene
LFNG
BRA
MEOX1
MESP1
CDX2
TCF15
MESP2
Normalised Gene Expression (z-score)
Section (A -> P)
Section (A -> P)
i
CS8 ~Day 17-19
CS9 ~Day 19-21
Head Folds
Node
Primitive Streak
Head Folds
Somites
PSM
Node
Primitive Streak